Systematic investigations into the role of ceramide subclass composition on lipid organization and skin barrier

Nadaban, A.

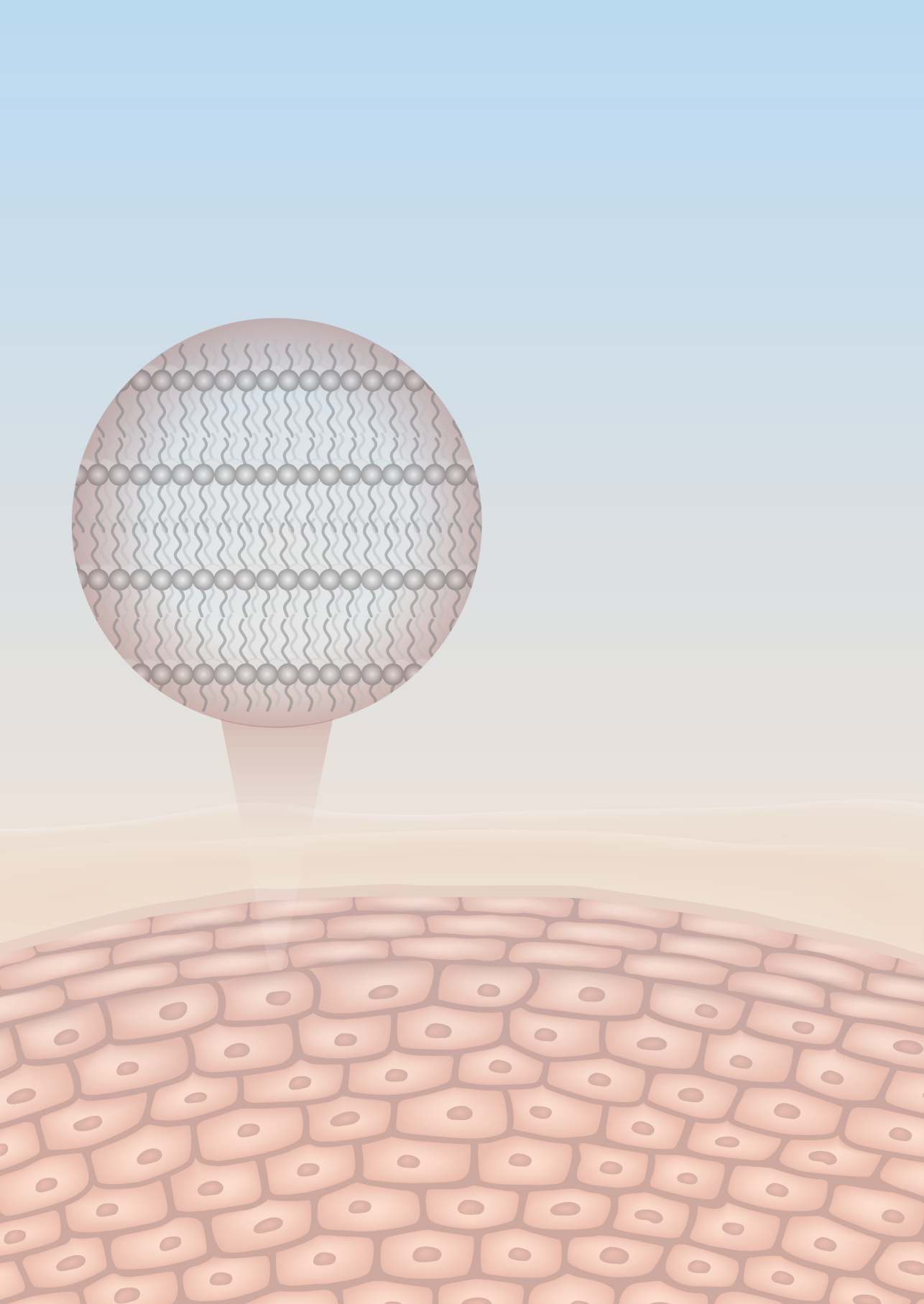

CHAPTER 6

The molecular arrangement of ceramides in the unit cell of the long periodicity phase of stratum corneum models shows a high adaptability to different ceramide head group structures

Authors and affiliations:
Andreea Nădăban[1], Gerrit S. Gooris[1], Charlotte M. Beddoes[1], Robert M. Dalgliesh[2], Marc Malfois[3], Bruno Demé[4], Joke A. Bouwstra[1*]

[1]Division of BioTherapeutics, Leiden Academic Centre for Drug Research, Leiden University, Leiden, The Netherlands
[2]ISIS Neutron and Muon Source, Science and Technology Facilities Council, Rutherford Appleton Laboratory, Didcot, United Kingdom
[3]ALBA Synchrotron, Cerdanyola del Vallès, Barcelona, Spain
[4]Institut Laue-Langevin, Grenoble, France

Submitted to BBA – Biomembranes (November 2023)

ABSTRACT

The stratum corneum (SC) lipid matrix, composed primarily of ceramides (CERs), cholesterol and free fatty acids (FFA), has an important role for the skin barrier function. The presence of the long periodicity phase (LPP), a unique lamellar phase, is characteristic for the SC. Insight into the lipid molecular arrangement within the LPP unit cell is imperative for understanding the relationship between the lipid subclasses and the skin barrier function. In this study, the impact of the CER head group structure on the lipid arrangement and barrier functionality was investigated using lipid models forming the LPP. The results demonstrate that the positions of CER *N*-(tetracosanoyl)-sphingosine (CER NS) and CER *N*-(tetracosanoyl)-phytosphingosine (CER NP), two essentials CER subclasses, are not influenced by the addition of another CER subclass (*N*-(tetracosanoyl)-dihydrosphingosine (CER NdS), *N*-(2R-hydroxy-tetracosanoyl)-sphingosine (CER AS) or D-(2R-hydroxy-tetracosanoyl)-phytosphingosine (CER AP)). However, differences are observed in the lipid organization and the hydrogen bonding network of the three different models. A similar localization of CER NP and CER NS is also observed in a more complex lipid model, with the CER subclass composition mimicking that of human SC. These studies show the adaptability and insensitivity of the LPP unit cell structure to changes in the lipid head group structures of the CER subclasses.

INTRODUCTION

The barrier function of the skin is mainly provided by the stratum corneum (SC), the uppermost layer of the skin (1). The SC consists of corneocytes embedded in a lipid matrix, with the latter representing the continuous pathway for permeation of compounds through the skin. Thus, the SC lipid matrix plays an important role to prevent undesired environmental compounds from entering the skin and to reduce excess water loss from the body (2). Ceramides (CER), free fatty acids (FFA) and cholesterol (CHOL) are the main SC lipid classes, present in an approximately equimolar ratio (3, 4). Phospholipids are not present in the SC, whereas they are prominently present in biological membranes of living cells (5). CERs are part of the sphingolipid family and play an important role in the regulation of cellular processes (6). Currently, 25 CER subclasses have been identified, with most of them having an acyl chain linked to a sphingoid base by an amide bond (7). All CER subclasses and FFAs have a wide chain length distribution.

The SC lipids are organized in two crystalline lamellar phases, a long periodicity phase (LPP) with a repeat distance of 13 nm and a short periodicity phase (SPP) with a repeat distance of 6 nm (8, 9). Previous studies have shown that the esterified ω-hydroxy ceramides (CER EO subclass) (Figure S1) are unique to the SC and are required for the formation of the LPP (10-12). In the absence of the CER EO subclass, primarily the SPP is formed (13). In some publications another lamellar phase has been reported in lipid model systems (14-17). However, there are no indications that this phase has been detected in SC. Within the lamellar phases in the SC, the lipid chains can adopt different packing densities, referred to as the lateral organization: orthorhombic (ordered phase, very dense packing), hexagonal (an ordered phase, but the lipid chains are less densely packed) or liquid phase (highly disordered phase) (18-20). The lipids in the SC lipid matrix are predominantly organized in an orthorhombic phase, with a fraction of the lipids adopting a hexagonal packing. The formation of liquid phase domains has also been reported for lipids in the SC (21).

Lipid model systems that resemble the lipid organization in the native SC provide detailed insight about the interactions between the different lipid subclasses. Previous studies used isolated human or porcine CERs mixed with synthetic FFAs and CHOL to prepare lipid models, which had a similar lipid organization to native SC (22-24). In subsequent studies, fully synthetic focused on lipid models were prepared with a synthetic CER composition mimicking the porcine or human CER subclasses. These models formed the LPP and SPP, similar to the lipid systems with isolated CERs and the native SC (11, 25-27). The next step was incorporating a limited number of CER subclasses mixed with FFAs and CHOL, aiming to keep the same phase behavior. This is of importance as simple lipid models are an excellent tool to gain detailed insight about the molecular arrangement of the lipids in the system, as deuterated lipids can be included in the mixture. If the

appropriate CER subclasses are chosen for the composition, even with a few numbers of CER subclasses, these lipid models still resemble the lipid phase behavior of SC (26-30).

Due to the co-existing lamellar phases (LPP and SPP), the lipid arrangement in these models is difficult to investigate using neutron diffraction, because of the partial overlap of the diffraction peaks of the two lamellar phases in the neutron scattering profile. To exclusively form the LPP, the unique lamellar phase in SC, the concentration of the esterified ω-hydroxy sphingosine ceramide (CER EOS) has to be increased to 30 or 40 mol% of the CER composition (10, 11). When forming only this lamellar phase, much more detail can also be obtained using other methods, such as Fourier transform infrared spectroscopy (FTIR) and neutron diffraction. Increasing the CER EOS level does not change the molecular arrangement of the repeating unit of the LPP, it only increases the fraction of lipids forming the LPP (10, 31). The molecular arrangement of the SPP in lipid models with different compositions was previously modelled using molecular dynamics simulations (32-35).

Understanding the role of the lipid subclasses for the lipid organization is crucial for explaining the changes in lipid composition and organization in diseased skin. For this reason, the lipid arrangement of the LPP unit cell has been investigated. Small-angle neutron diffraction (SANS) can provide the localization of water molecules and deuterated lipids in the LPP unit cell, using contrast variation of D_2O/H_2O hydration buffers and deuterated compounds, while FTIR provides information about lipid domain forming and the neighboring lipid chains. Previous studies identified the location of CER EOS, CHOL, FFAs, CER *N*-(tetracosanoyl)-sphingosine (CER NS) and CER *N*-(tetracosanoyl)-phytosphingosine (CER NP) (Figure S1) in lipid models with different compositional complexity (30, 36-38). According to these studies the lipids are arranged in a trilayer in the LPP unit cell. The outer layers of the LPP consist of the acyl chain of CER EOS and the CHOL, while the FFAs and acyl chains of CER NP and CER NS are predominantly localized in the central layer of the LPP. CER NS and CER NP have been reported to mainly adopt a linear conformation, as depicted schematically in Figure S2.

In the present study the influence of *N*-(2R-hydroxy-tetracosanoyl)-sphingosine (CER AS C24), D-(2R-hydroxy-tetracosanoyl)-phytosphingosine (CER AP C24) and CER N-(tetracosanoyl)-dihydrosphingosine (CER NdS C24) (Figure S1) on the lipid organization and barrier function of lipids assembled in the LPP was investigated. First, a model with only CER EOS, CER NP, CER NS and one of these additional CER subclasses (CER AS, CER AP or CER NdS) together with CHOL and FFA was used. It was observed that the additional CER subclasses did not affect the positions of the acyl chain of CER NP and CER NS in the trilayer unit cell. Additional studies show that the two acyl chains are similarly positioned even in a complex model representing the human SC CER subclass composition, suggesting an insensitivity of the LPP to the CER subclass composition.

MATERIALS AND METHODS

Materials

The following synthetic CERs used in the study: *N*-(30-Linoleoyloxy-triacontanoyl)-sphingosine (CER EOS C30), *N*-(tetracosanoyl)-sphingosine (CER NS C24), *N*-(tetracosanoyl)-phytosphingosine (CER NP C24), *N*-(2R-hydroxy-tetracosanoyl)-sphingosine (CER AS C24), D-(2R-hydroxy-tetracosanoyl)-phytosphingosine (CER AP C24) and CER NS and CER NP with perdeuterated acyl chains (NSd47, NPd47) were kindly donated by Evonik (Essen, Germany). CER N-(tetracosanoyl)-dihydrosphingosine (CER NdS C24) was purchased from Avanti Polar Lipids (Alabama, USA). CHOL, palmitic acid (FFA C16), stearic acid (FFA C18), arachidic acid (FFA C20), behenic acid (FFA C22), lignoceric acid (FFA C24), D_2O and the acetate buffer salts were obtained from Sigma-Aldrich-Chemie GmbH (Schnelldorf, Germany). Deuterated FFA C24 (DFFA24) was acquired from Arc Laboratories B.V. (Apeldoorn, The Netherlands). Analytical grade organic solvents were purchased from Biosolve B.V. (Valkenswaard, The Netherlands). The nucleopore polycarbonate membranes were purchased from Whatman (Kent, UK).

Lipid compositions preparation

An equimolar ratio of CERs:CHOL:FFAs was used for all lipid compositions. The CER fraction contained CER EOS (40% of CER fraction), CER NS, CER NP and either CER AS, CER AP or CER NdS for the simple models (CERs structures presented in Figure S1). The composition of the models mimicking human CER model is indicated in Table 1 by Human. This is based on the human model investigated by Uche et al. (21), but the concentration of CER EOS was increased to 40 mol% of total CERs in this study, to avoid the simultaneous formation of the LPP and SPP. The FFA composition of the Human model is denoted by FFA5 and consists of FFAs with chain lengths of C16, C18, C20, C22 and C24 (at molar percentages of 1.8, 4.0, 7.6, 47.8, 38.8%). Deuterated models were prepared by replacing CER NS, CER NP and FFA C24 (or FFA5) with their deuterated counterparts (indicated in the model names and in bold).

The details for the sample preparation used for each biophysical technique are provided in Table 2. The lipids were dissolved in the appropriate solvent at a concentration of 5 mg/ml, then a Camag Linomat IV device (Muttenz, Switzerland) was used to spray the lipids under a gentle stream of nitrogen (spraying rate 14 s/µl) around 1 mm from the support. An automatic equilibrator was then used at a heating rate of 4°C/min until a temperature of 95°C was reached (for the models with CER AS, CER AP or CER NdS). The sample was maintained at this temperature for 65 min, then slowly cooled to 25°C. For the Human models, the equilibration temperature was 85°C, maintained for 30 min, which was high enough to ensure the melting of the lipids.

Table 1. Lipid models used in this study, with deuterated lipids indicated in bold

Sample name	Composition	Molar ratio
LPP NS:NP:AS	EOS C30: NS C24: NP C24: AS C24: CHOL: FFA C24	0.4: 0.15:0.15:0.3: 1: 1
LPP NS:NP:AP	EOS C30: NS C24: NP C24: AP C24: CHOL: FFA C24	0.4: 0.15:0.15:0.3: 1: 1
LPP NS:NP:NdS	EOS C30: NS C24: NP C24: NdS C24: CHOL: FFA C24	0.4: 0.15:0.15:0.3: 1: 1
LPP NSd47:NP:AS	EOS C30: **NS C24-d47:** NP C24: AS C24: CHOL: FFA C24	0.4: 0.15:0.15:0.3: 1: 1
LPP NS:NPd47:AS	EOS C30: NS C24: **NP C24-d47:** AS C24: CHOL: FFA C24	0.4: 0.15:0.15:0.3: 1: 1
LPP NSd47:NP:AP	EOS C30: **NS C24-d47**: NP C24: AP C24: CHOL: FFA C24	0.4: 0.15:0.15:0.3: 1: 1
LPP NS:NPd47:AP	EOS C30: NS C24**: NP C24-d47**: AP C24: CHOL: FFA C24	0.4: 0.15:0.15:0.3: 1: 1
LPP NSd47:NP:NdS	EOS C30: **NS C24-d47**: NP C24: NdS C24: CHOL: FFA C24	0.4: 0.15:0.15:0.3: 1: 1
LPP NS:NPd47:NdS	EOS C30: NS C24: **NP C24-d47:** NdS C24: CHOL: FFA C24	0.4: 0.15:0.15:0.3: 1: 1
LPP NSd47:NPd47:AS:DFFA	EOS C30: **NS C24-d47: NP C24-d47**: AS C24: CHOL: **DFFA C24**	0.4: 0.15:0.15:0.3: 1: 1
LPP NSd47:NPd47:AP:DFFA	EOS C30: **NS C24-d47: NP C24-d47**: AP C24: CHOL: **DFFA C24**	0.4: 0.15:0.15:0.3: 1: 1
LPP NSd47:NPd47:NdS:DFFA	EOS C30: **NS C24-d47: NP C24-d47**: NdS C24: CHOL: **DFFA C24**	0.4: 0.15:0.15:0.3: 1: 1
Human	EOS C30: NS C24: NP C24: AS C24: NdS C24: AP C24: CHOL: FFA5	0.4: 0.09: 0.22: 0.09: 0.09: 0.11 : 1: 1
Human-NSd47	EOS C30: **NS C24-d47**: NP C24: AS C24: NdS C24: AP C24: CHOL: FFA5	0.4: 0.09: 0.22: 0.09: 0.09: 0.11 : 1: 1
Human-NPd47	EOS C30: NS C24: **NP C24-d47**: AS C24: NdS C24: AP C24: CHOL: FFA5	0.4: 0.09: 0.22: 0.09: 0.09: 0.11 : 1: 1

Table 2. Sample preparation information for each analytical technique

Technique	Lipid amount	Solvent	Support	Spraying area	Hydration
SAXD	1 mg	hexane/ ethanol (2:1, v/v)	nucleopore polycarbonate membrane	2 x 3 mm^2	24 h, 80% relative humidity, 25°C
FTIR	1 mg	chloroform/ methanol (2:1, v/v)	silver bromide window	1 x 1 cm^2	≥12 h, acetate buffer in D_2O (pH 5), 37°C
SANS	10 mg	chloroform/ methanol (2:1, v/v)	silicon substrate	1.2 x 3.8 cm^2	≥12 h, D_2O/H_2O buffer (100%, 50%, 8%), 37°C
TEWL	1 mg	hexane/ ethanol (2:1, v/v)	nucleopore polycarbonate membrane	1 x 1 cm^2	30 min, 25°C

The samples were hydrated before the measurements. The different techniques required individual hydration methods; however, the phase behavior was not affected by the difference in hydration method.

Small-angle X-ray diffraction (SAXD)

SAXD measurements were performed at the ALBA Synchrotron (Barcelona, Spain), using the NCD-SWEET beamline, with a Pilatus 1M detector with a pixel array 981 × 1043 (pixel size 172 × 172 μm^2). The wavelength of the X-ray beam was 0.999 Å and the sample to detector distance was 2.148 m. Silver behenate was used as a calibration of the set-up. Two samples were measured for each composition, with each sample scanned for 20 s, at 23°C. The one-dimensional SAXD profiles of the scattering intensity as a function of the scattering vector (q) were obtained after the integration of the two-dimensional scattering plot, over a 90° segment from the beam center. The scattering vector (q) was calculated using the formula: $q = (4\pi \sin\theta)/\lambda$, where θ represents the scattering angle and λ is the wavelength. The peak positions (q_n) were determined by peak fitting in Fityk (Pearson VII function) (39). Least square fitting was used to calculate the repeat distance of the lamellar phase (d), as follows: $d = 2n\pi/q_n$, where n is the diffraction peak order number.

FTIR

A PerkinElmer Frontier FTIR (PerkinElmer, Waltham, USA), with a nitrogen cooled mercury cadmium telluride detector, was used for FTIR data collection. The sample compartment was continuously purged with a dry air flow to remove moisture from the environment. Each spectrum represents 77 interferograms collected with a resolution of 1 cm^{-1}, in the wavenumber range 500 - 4000 cm^{-1}. The samples were measured between 10 and 90 °C, at a heating rate of 4 min/°C. The extraction of the spectra was performed in TimeBase (Perkin Elmer, Waltham, USA) and the processing in Spectrum (Perkin Elmer, Waltham, USA). Data processing included deconvolution (γ = 2.2) and smoothing of the spectra (factor 76.7%). Three measurements were performed for each lipid model.

The CH_2 symmetric stretching vibrations (ν_sCH_2, ~2849 cm^{-1}) provide information about the conformational ordering. The deuterated CD_2 stretching vibration occurs at ~2090 cm^{-1} (ν_sCD_2). The ν_sCH_2 and ν_sCD_2 vibrations are measured in the temperature range 10-90°C. The midpoint transition temperature represents the average temperature the lipids are transitioning from orthorhombic to hexagonal packing (T_MO-H) or from hexagonal to liquid (T_MH-L) packing, calculated as previously described (40). The CH_2 and CD_2 scissoring vibrations (δCH_2, 1462-1473 cm^{-1}; δCD_2, 1085-1095 cm^{-1}) provide information about the lipid chain packing. The peak positions of the δCH_2 and δCD_2 vibrations at 10°C and the peak heights were determined using Python scripts. A peak height ratio (OR/MID) was calculated as the ratio of the average peak height of the two orthorhombic peaks and the height of the central peak. The exact positions of the amide I

vibration (~1650 cm^{-1}) and amide II vibration (~1550 cm^{-1}) were also determined by peak fitting.

Neutron diffraction at ISIS Neutron and Muon Source

Neutron diffraction measurements of the LPP NS:NP:AS, LPP NS:NP:AP and LPP NS:NP:NdS models were performed on the LARMOR instrument at ISIS Neutron and Muon Source (Rutherford Appleton Laboratory, UK). The neutron beam wavelength range was 1 – 12.5 Å and the sample – detector distance was 4.4 m. The angle of the sample to the beam was 2.5° and the detector was set at a 2θ angle of 5° to the direct beam (area covered 664 × 600 mm; pixel size 4 × 8 mm). The sample environment was an aluminum chamber and an empty chamber was used for background measurement (subtracted from the scattering profile of each sample). The samples were measured at each hydration buffer (100%, 50% and 8% D_2O/H_2O) for 4 h (40 μA/h accelerator proton charge) at 25°C. A direct beam measurement was used for the normalization to the incident flux shape and the detector efficiency.

The Mantid software was used for reducing the data and normalizing the intensity as a function of the scattering vector (q) (41). The resulting q-range was 0.032 – 0.991 nm^{-1}. The Bragg equation was used to convert the scattering angle (2θ) to q: $q = 4\pi sin\theta \,/\, \lambda$. Based on the positions of the equidistant Bragg peaks, the repeat distance (d) of the lamellar phase was calculated: $d = 2\pi n/q_n$; with n representing the diffraction order number of the peak at the position q_n.

Next, the scattering length density profiles (SLD) were determined for each sample, using the data analysis procedure previously described (36, 37). The intensity of each diffraction order was obtained by fitting the Bragg peaks (Fityk software, with a Pearson VII function) (39). Next, the structure factor amplitude for each diffraction order ($|F_n|$) was determined using the formula: $\left|F_n\right| = A_n\sqrt{LI_n}$, where L represents the Lorentz correction factor, which can be assumed equal to q, due to the high degree of lipid lamellae orientation. A_n, the correction factor for the sample absorption, was calculated with the formula below, where l is the thickness of the lipid sample and μ is the linear attenuation coefficient (42):

$$A_n = \frac{1}{\sqrt{\frac{sin\theta}{2\mu l}\left(1-e^{\frac{-2\mu l}{sin\theta}}\right)}}$$

The D_2O/H_2O contrast variation method was used for the determination of the water profile phase signs. These phase signs are obtained from the positive or negative signs of the slope of the difference between the absolute structure factors $|F_n|$ of the sample hydrated at 100% and 8% D_2O/H_2O, as previously described (38). Assuming that the lipid head groups are located at the unit cell boundary, the water molecules are located close to the hydrophilic lipid head groups at the cell boundary as well. This assumption results in the phase signs for the water profile of the LPP NS:NP:AS, LPP NS:NP:AP and LPP

NS:NP:NdS protiated samples - + - + - +. Then, the F_n with the corresponding phase signs are plotted as a function of the D_2O/H_2O buffer ratio (Figure S3). The centrosymmetric structure of the LPP is indicated by the linear fitting obtained from plotting the F_n values as a function of D_2O/H_2O buffer for all samples (36, 37).

The phase signs of the protiated and deuterated lipid samples were individually determined based on the positive or negative sign of the F_n at 8% D_2O/H_2O buffer (Figure S3). We chose to use the data obtained using 8% D_2O/H_2O as at this composition the total scattering contribution of the water molecules is zero. As can be observed in Figure S3, for all protiated and deuterated samples the resulting phase signs combination was - + - + - +.

The scattering length density profile (SLD) of the LPP unit cell was obtained by Fourier reconstruction using the structure factor values and the phase signs with the following equation (x is the distance in the unit cell, x=0 represents the center of the unit cell):

$$\rho(x) = F_0 + 2\sum_{n=1}^{n_{max}} F_h \cos\left(\frac{2\pi n x}{d}\right)$$

The scattering density per unit volume (F_0) was determined using the density of the lipid sample and its chemical composition and it included one water molecule per lipid (43). By subtracting the SLD profile of the protiated sample from the SLD profile of the deuterated sample (both hydrated at 8% D_2O/H_2O, as the contribution of the buffer to the SLD is 0 at this ratio), the SLD profile of the deuterated moiety is obtain. This resulting SLD profile indicates the location of the deuterated lipid chain in the LPP unit cell.

The "relative absolute" SLD data were calculated following the steps previously described (36, 37, 44). Based on previous measurements using the same LARMOR instrument settings and composition with CER NS with a sphingosine deuterated (CER NSd7), a scaling factor (S_f) was introduced, calculated as the ratio between the peak areas of the NSd7 and NPd47 chains of the CER EOS/CER NS/CER NP model (38). The peak area of the SLD profile of NPd47 chain (fitted for the LPP NS:NPd47:NdS model from this study) was then multiplied by S_f to obtain the corrected NPd47 peak area, scaled to previous measurements (SLD_{area}). The factor for calculating the "relative absolute" SLD values ($SLD_{correct}$) is the ratio between the scattering of the deuterium atoms in the NPd47 chain (SLD_{dif}) and the corrected peak area of the NPd47 SLD (SLD_{area}). SLD_{dif} is the difference between the scattering of a deuterated CER acyl chain ($C_{23}D_{47}$) and the protiated CER acyl chain ($C_{23}H_{47}$). The $SLD_{correct}$ factor was applied to the scattering factor F_n values, transforming the data to the "relative absolute" scale.

Neutron diffraction at the Institut Laue-Langevin

The molecular arrangement in a lipid model with a composition mimicking the human SC was examined as well. Neutron diffraction measurements were performed on the protiated model and the models with either the deuterated acyl chain of CER NS or CER NP, to examine the location of these two chains in the LPP unit cell. These membrane diffraction measurements were performed at the D16 small-angle neutron diffractometer,

at Institut Laue-Langevin (ILL, Grenoble, France), as previously described (30, 36, 37, 45). In short, the incoming slit-collimated beam, with a wavelength of 4.45 Å, was set at 30 mm vertically and 3 mm horizontally, to ensure the proper illumination of the sample during data collection of all the diffraction orders. The diffraction patterns were measured in reflection mode, using MILAND, a ^{3}He detector (320 x 320 mm; special resolution of 1 x 1 mm), with a sample to detector distance of 0.95 m.

Each sample was mounted in an aluminum humidity chamber (46), maintained at 25°C and 99% RH and measured for 4 h (for the 100% and 50% D_2O/H_2O hydration buffers) and 9 h (for the 8% D_2O/H_2O buffer), depending on the signal to noise ratio. The samples were rotated (Ω axis) between 0.05 and 10.2° (in steps of 0.05°) at a detector angle (γ) of 11.2° (in the Ω range 0.05 - 2.25°), to separate the first and second order from the direct beam, and 12° (Ω range 1.8 - 10.2°), to cover the second to ninth diffraction orders of the LPP. For each diffraction order, the scans were measured at the specular angle ± 0.1° (total of 5 scans), which were then averaged and fitted. The scattering data were reduced, the background (empty aluminum chamber) was subtracted and the peaks were fitted using the processing software LAMP (47). The data were converted from the scattering angle 2θ to q-values using the Bragg equation: $q = 4\pi sin\theta \,/\, \lambda$. The SLD calculation was further performed as described above. The linear fitting of the structure factor F_n values as a function of the D_2O/H_2O ratio is illustrated in Figure S4.

Trans-epidermal water loss (TEWL)

To measure TEWL values, the lipid samples were mounted in Permegear in-line diffusion cells (Bethlehem, USA), with a diffusion area of 0.28 cm^2. The acceptor compartment was filled with MiliQ water and the donor compartment was empty. TEWL was monitored using the AquaFlux AF200 device (Biox Systems Ltd., London, UK), which was connected to the diffusion cells using a measurement cap. The TEWL flux was measured each 10 s for 30 mins. The steady-state TEWL was calculated as an average of the values obtained during the last 10 min of the 30 mins measurement period. At least six samples were measured for each composition. GraphPad Prism 8 was used for statistical analysis (one-way ANOVA test with Bonferroni correction; $P < 0.05$ and t test for comparisons of two groups; $P < 0.05$).

RESULTS AND DISCUSSION

Lamellar and lateral organization

The lamellar organization of the LPP simple models was investigated with SAXD. The X-ray diffraction profiles of the LPP NS:NP:NdS, LPP NS:NP:AS and LPP NS:NP:AP models display seven equidistant peaks corresponding to a lamellar phase with the repeat distance of 12.6, 12.7 and 12.9 nm, respectively (Figure 1). The diffraction peak intensity distribution

(second order with the highest intensity, followed by the first and then the third order) is characteristic for the LPP (31). The increase in repeat distance is in agreement with the findings of Uche et al. (48). They reported repeat distances of models with CER EOS (40m/m%) and either CER NS, CER NP, CER AS or CER AP (60m/m%) mixed with CHOL and FFAs; an increase in the LPP repeat distance was observed when comparing the EOS/AS (12.6 nm) and EOS/AP (13.4 nm) models. A peak at q= 1.8 nm^{-1} is detected in all samples and it corresponds to phase-separated crystalline CHOL. The peaks of the LPP NS:NP:NdS and LPP NS:NP:AS models are generally sharp, however, for the LPP NS:NP:AP model the peaks corresponding to the third, fourth and sixth diffraction orders are slightly asymmetric, indicating that an additional phase might be present.

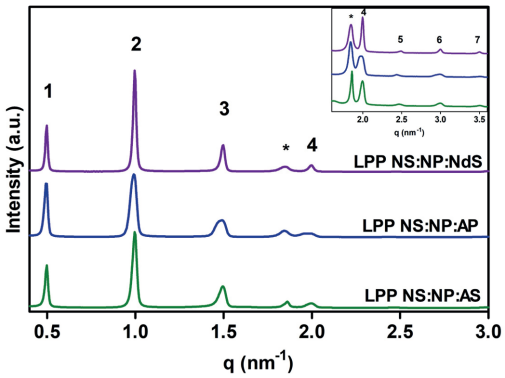

Figure 1. The SAXD profiles of the three lipid models (LPP NS:NP:NdS in purple, LPP NS:NP:AP in blue and LPP NS:NP:AS in green). The insert displays the zoomed in q-range 1.6 – 3.6 nm^{-1}. The LPP diffraction orders are depicted with Arabic numbers and phase separated (crystalline) CHOL is denoted with the asterisk (*).

Next, the lateral organization was examined using FTIR. Figure 2A displays the δCH_2 vibrations of the LPP NS:NP:NdS, LPP NS:NP:AS and LPP NS:NP:AP models and Figure 2B the thermotropic behavior of the $\nu_s CH_2$ vibrations. The peak splitting indicates the presence of an orthorhombic packing in all three compositions. The position of the δCH_2 vibration peaks was determined by peak fitting. From the positions the δCH_2 peaks, the splitting distance (distance between the two δCH_2 peaks) was determined and this distance was around 10.6 cm^{-1}. In comparison, pure FFA C24 has maximum δCH_2 peak splitting of 10.7 cm^{-1} (unpublished), thus this denotes that the size of the orthorhombic domains in the three models is close to maximum splitting indicating large domain sizes of at least 100 lipid molecules (49, 50). In addition, a δCH_2 peak height ratio was calculated (OR/MID) as the ratio of the two orthorhombic peaks heights and the central (middle) peak height (Table 4). This is of interest as a higher fraction of hexagonal packing (peak position at around 1467 cm^{-1} thus attributing to the MID peak) will result in a shallower dip and thus a lower height ratio of OR/MID peaks. The OR/MID height ratio of the LPP

NS:NP:AP model is 2.5, smaller than the other models (2.9 and 3.3), suggesting that a larger fraction of the lipids in this AP model is hexagonally packed in comparison to the other two models, but the size of the orthorhombic domains is very similar in the three models. Uche et al. reported an increased hexagonal phase in a model with CER EOS/CER AP (40/60 mol%) in comparison with a similar model with either CER AS, CER NS or CER NP (48). This showed a similar tendency as the models examined in this study.

The thermotropic curves of the $\nu_s CH_2$ vibrations of the LPP NS:NP:NdS, LPP NS:NP:AS and LPP NS:NP:AP models are plotted in Figure 2B. At 10°C, the $\nu_s CH_2$ wavenumbers of all models are <2849 cm^{-1}, which demonstrates a high conformational ordering of the lipids corresponding to an orthorhombic lipid packing, as shown by the δCH_2 vibrations shown in Figure 2A at 10°C. This remains stable up to ~32°C when a transition is indicated by the increase of the $\nu_s CH_2$ wavenumber to ~2850 cm^{-1}. This represents the phase transition from orthorhombic to a less ordered phase, probably a hexagonal packing.

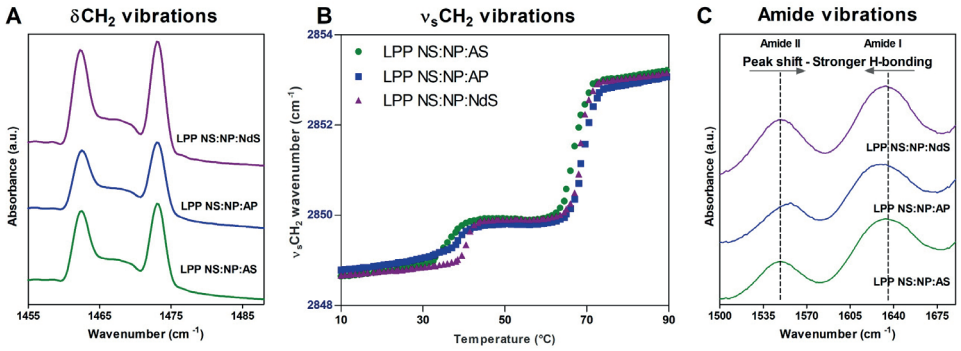

Figure 2. (A) δCH_2 vibrations of the LPP NS:NP:NdS, LPP NS:NP:AP and LPP NS:NP:AS, measured by FTIR at 10°C. (B) Thermotropic plots of the three samples with the wavenumbers of the $\nu_s CH_2$ frequencies displayed in the temperature range 10-90°C. (C) FTIR spectrum of the region 1500 – 1680 cm^{-1}, displaying the two amide vibrations at 10°C. The data for each lipid model represents an average of three separate measurements.

Figure S5 shows the δCH_2 vibrations at 25°C (temperature used for the other methods: SANS, TEWL) and at 40°C. At 25°C the two δCH_2 peaks are still fairly well separated, with the distance between the peaks of 10.2 cm^{-1} for the LPP NS:NP:NdS model, while for the LPP NS:NP:AS and LPP NS:NP:AP models, it was 9.9 and 9.7 cm^{-1} respectively. The peak splitting distance at 25°C is lower in comparison with the 10°C measurements (Table 3), and the same trend is observed for the OR/MID peak height ratio at 25°C (OR/MID ratio values are 1.6 ± 0.1, 1.9 ± 0.1 and 2.9 ± 0.1 for the LPP NS:NP:AS, LPP NS:NP:AP and LPP NS:NP:NdS respectively). As it can be seen from Figure S5B, at 40°C the δCH_2 vibrations show a broader peak with a shoulder, indicating the ongoing transition to the hexagonal packing of the lipids.

The mid-phase transition temperatures (Table 3) reveal small differences between the three models, especially for the orthorhombic to hexagonal phase transition (T_MO-H). This transition in the LPP NS:NP:NdS model occurs at a higher temperature (40.8 ± 0.3 °C) compared to the other two models, which have similar mid-transition temperatures (36.2 ± 1.4 °C and 38.7 ± 0.6 °C for LPP NS:NP:AS and LPP NS:NP:AP models respectively). The differences in the mid-phase transition temperatures explain the OR/MID δCH_2 peak height ratios observed at 25°C. The LPP NS:NP:NdS model shows the least differences in comparison to the values obtained at 10°C, due to the higher phase transition temperature to a hexagonal phase in this model.

The hexagonal to liquid phase transitions occur in comparable temperature ranges and the T_MH-L shows no significant differences between the three models (Table 3). The lipid mixing is followed using partially deuterated samples and this is described below.

Table 3. Midpoint transition temperatures for the three models, the δCH_2 scissoring peak distances and the peak positions of the amide I and II vibrations. Data are shown as averages with standard deviations for 3 repeat measurements.

Lipid sample	δCH_2 peak distance (cm^{-1})	δCH_2 OR/MID peak height ratio	T_MO-H (°C)	T_MH-L (°C)	Amide peak position (cm^{-1})
LPP NS:NP:AS	10.7 ± 0.1	2.9 ± 0.1	36.2 ± 1.4	67.3 ± 0.7	1547.0 ± 0.9 1635.8 ± 0.1
LPP NS:NP:AP	10.6 ± 0.1	2.5 ± 0.3	38.7 ± 0.6	69.1 ± 0.9	1548.1 ± 0.3 1627.5 ± 0.1
LPP NS:NP:NdS	10.8 ± 0.1	3.3 ± 0.1	40.8 ± 0.3	68.6 ± 0.3	1547.3 ± 0.2 1632.6 ± 0.4

Hydrogen bonding network in the models

The head group structure of the various CER subclasses investigated is different among the models, as CER NdS, CER AS and CER AP have a different number of hydroxyl groups. These CERs can act as both hydrogen bond donor and/or acceptor, thus FTIR studies focusing on amide vibrations can provide information about hydrogen bonding network in the systems. The amide I vibration (~1650 cm^{-1}) results from the C=O stretching vibration and the amide II (~1550 cm^{-1}) vibration is determined by both the N-H bending and C-N stretching vibrations. If the position of the two amide vibrations is closer (when the amide I has a lower frequency and amide II a higher frequency), this indicates a stronger hydrogen bonding (51, 52). In the simple LPP models the amide I and II vibrations are characterized by broad peaks (Figure 2C). The exact peak positions have been determined by peak fitting (Table 3). The LPP NS:NP:NdS and LPP NS:NP:AS models have a similar distance between the amide I and II vibrations, indicating a similar hydrogen bonding network (Figure 2C). However, the LPP NS:NP:AP model shows a higher frequency for the amide II peak and lower amide I frequency, resulting in a smaller distance between the two peaks. This indicates that the inclusion of CER AP in the lipid model results in a

stronger hydrogen bonding, in comparison with the other two models, but this is not surprising as the head group of CER AP contains four hydroxyl groups.

The difference in hydrogen bonding is in agreement with previous studies, which reported stronger hydrogen bonding for phytosphingosine-based CERs than for the sphingosine-based CERs, in single component systems, in three components systems, as well as in model systems forming the LPP (48, 52, 53). It is likely that both the concentration of CER AS, CER AP or CER NdS in this study (30 mol% of total CERs) and the composition of the models, leads to a weaker hydrogen bond network than in single component CER systems.

Lipid barrier measured by trans-epidermal water loss (TEWL)

TEWL measurements were performed to examine the lipid barrier changes after adding an extra CER subclass to the mixture, with the TEWL of the three models with either CER AS, CER NdS or CER AP being compared with the model with the composition CER EOS, CER NS, CER NP, CHOL, FFA C24 (LPP NS:NP 1:1). (Figure 3). The lipid organization of this LPP NS:NP 1:1 model was reported in a previous study and it can be considered a control sample (38). The TEWL of the LPP NS:NP:AS and LPP NS:NP:AP models is significantly increased compared to the LPP NS:NP 1:1 model, while there is no significant difference for the TEWL flux of LPP NS:NP:NdS model compared to the control model (one-way ANOVA test). The LPP NS:NP:AS model showed a poorer barrier function compared to the LPP NS:NP:AP model as well, as shown by the significant differences in the TEWL (t test of the two groups).

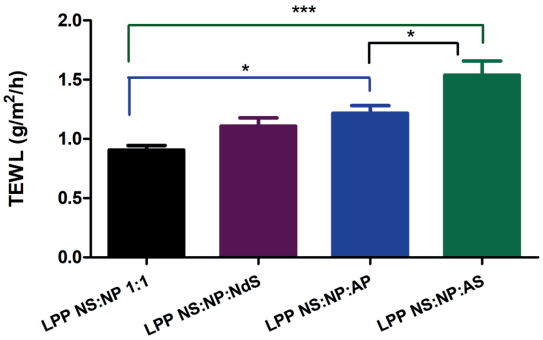

Figure 3. Trans-epidermal water loss of the models, calculated as an average of the steady flux in the last 10 min of the measurements. Data are shown as averages with standard deviations of n≥6 measurements of different lipid membranes per group (* P<0.05; *** P<0.005)

There are at least two factors that play a role in the permeability of the lipid barrier in comparing these systems: hydrogen bonding and the fraction of lipids organized in hexagonal packing. The hydrogen bond network might have an important role for the barrier function, as a dense hydrogen network might reduce the permeation of water

molecules through the lipid layers and this would lead to a lower TEWL. However, the presence of a larger fraction of lipids adopting a hexagonal packing might enhance the permeation of molecules though the lipid layer, causing a reduced lipid barrier (54). As shown in Figure S5A (Supplemental Material), at 25°C the LPP NS:NP:NdS model has a higher fraction of orthorhombically packed lipids compared to the LPP NS:NP:AS and LPP NS:NP:AP models. Thus, this small packing difference between the models, as well as the stronger hydrogen bond network of CER AP in comparison with the other two models, explains the trend observed for the TEWL, with the highest permeability to water measured for the LPP NS:NP:AS model.

Differences in the permeability of LPP models with different CER head group structure were also observed by Uche et al. in a previous study, where phytosphingosine-based CER models (with CER AP or CER NP) showed a lower permeability than the sphingosine-based CER models (CER AS or CER NS) (48). In models forming only the SPP, a study by Kováčik et al. indicates a higher water loss of the CER NP model compared to the CER NS model, with no differences between the models involving CER AP, CER AS or CER NdS (55). The different results compared to our finding are probably due to extensive phase separation in these models that also affect the packing of the lipids.

Molecular arrangement of the LPP unit cell

Neutron diffraction measurements were carried out for the protiated models (LPP NS:NP:AS, LPP NS:NP:AP and LPP NS:NP:NdS) and the models that included either the deuterated acyl chain of CER NS (NSd47) or CER NP (NPd47) to identify the effect of the CER AS, AP and NdS on the position of the deuterated acyl chains in the LPP unit cell. The one-dimensional scattering intensity plots (Figure S6, Supplemental information) showed a sequence of six equidistant peaks identified as the LPP diffraction orders. Apart from there, there is a peak at 1.8 nm^{-1}, corresponding to crystalline CHOL (phase separated) but there was no overlap with the peak corresponding to the fourth LPP diffraction order. As noted in the SAXD plots, the diffraction peaks of the LPP NS:NP:AP model are broader, but no co-existing phases were detected.

After the structure factors and corresponding phase signs were determined for each sample, the SLD profiles were obtained. The SLD profiles of the water were determined by subtraction of the SLD intensity of the protiated sample equilibrated and measured at 100% D_2O/H_2O and at 8% D_2O/H_2O hydration. Figure 4A, D, G display the water SLD profiles of the three models. Two regions of high intensity are present at the border of the LPP unit cell (at approximately 6.3 nm from the center of the unit cell). Besides these, there are also two inner water regions located at 2.2 ± 0.1 nm from the unit cell center. The position of the water molecules is near the lipid head group regions (and not next to the hydrophobic lipid tails), therefore the water SLD profile demonstrates that the trilayer structure of the LPP is centrosymmetric, as previously reported (36, 37).

Next, we determined the acyl chain locations of CER NS and CER NP in the unit cell. The SLD profiles of the deuterated NSd47 and NPd47 chains were calculated by subtracting the SLD profile of the protiated sample from the deuterated samples, hydrated with the 8% D_2O/H_2O buffer. The resulting SLD profiles represent the localization of the acyl chains of CER NS or CER NP in the LPP unit cell (Figure 4 B,C,E,F,H and I). The LPP NS:NPd47:NdS model is characterized by an increased intensity of the SLD in the middle of the unit cell, as well as an elevation at the outer layers (Figure 4B). Thus, the deuterated acyl chains of CER NP are positioned mainly in the central layer of the LPP, while a small part of the lipid chains are located at the unit cell boundaries. The LPP NSd47:NP:NdS model shows the same intensity distribution in the SLD profile, suggesting the same position for the acyl chains of CER NS and CER NP in the unit cell of the LPP (Figure 4C).

Examining the SLD profiles of the LPP NS:NPd47:AP and LPP NSd47:NP:AP lipid models (Figure 4E,F), as well as LPP NS:NPd47:AS and LPP NSd47:NP:AS systems (Figure 4H,I), the same SLD distribution is present as for the LPP NS:NP:AP samples, indicating the same location of the deuterated acyl chains of CER NP and CER NS in these unit cells (primarily in the inner layer of the unit cell of the LPP, with a small part of the chains at boundary of the unit cell). The percentage of deuterated CERs in each model is the same (15 mol% of CER content, which represents ~5 mol% of total lipids) and the relative absolute intensities of the six SLD profiles are similar between the lipid models, suggesting the same distribution of the deuterated chains is present in all the systems.

These results indicate that the addition of another CER in a simpler LPP NS:NP model does not influence the arrangement of CER NS and CER NP in the unit cell of the LPP. The location of these two CERs is the same as reported in previous studies of lipid models that form the LPP (30, 36, 38, 56). These studies used both simple lipid models comprising of only two or three CERs (CER EOS, CER NS and CER NP) and a more complex model with a CER composition mimicking the pig SC composition.

The CER AS, CER NdS and CER AP that were included in this study have the same chain length as CER NS and CER NP (24 carbon atoms). As the molecular arrangement of CER NS or CER NP is not affected by including one of these three CERs, this demonstrates that the LPP arrangement is insensitive to changes in CER subclass. Previous studies showed that replacing 75 mol% of long chain CER NS (C24) with short chain CER NS (C16) in a LPP model influences the lipid organization (57). Thus, it is likely that this would influence the molecular arrangement in the LPP as well. Furthermore, Beddoes et al. concluded that the CER headgroup structure has an important role for the molecular lipid arrangement in the LPP unit: when a proportion of the CERs is replaced with FFAs (with the same chain length as the CER), a redistribution of the CERs can occur (45). Therefore, the presence of the CER head group is important but changing the nature of the CER head group has no effect on the lipid molecular arrangement in the LPP unit cell.

The position of CER AS, CER AP or CER NdS could not be identified in this study due to the unavailability of these deuterated acyl chains of the CER subclasses commercially. However, important information about their location can be obtained when examining the lipid chain interactions, by performing FTIR studies as described in the next section.

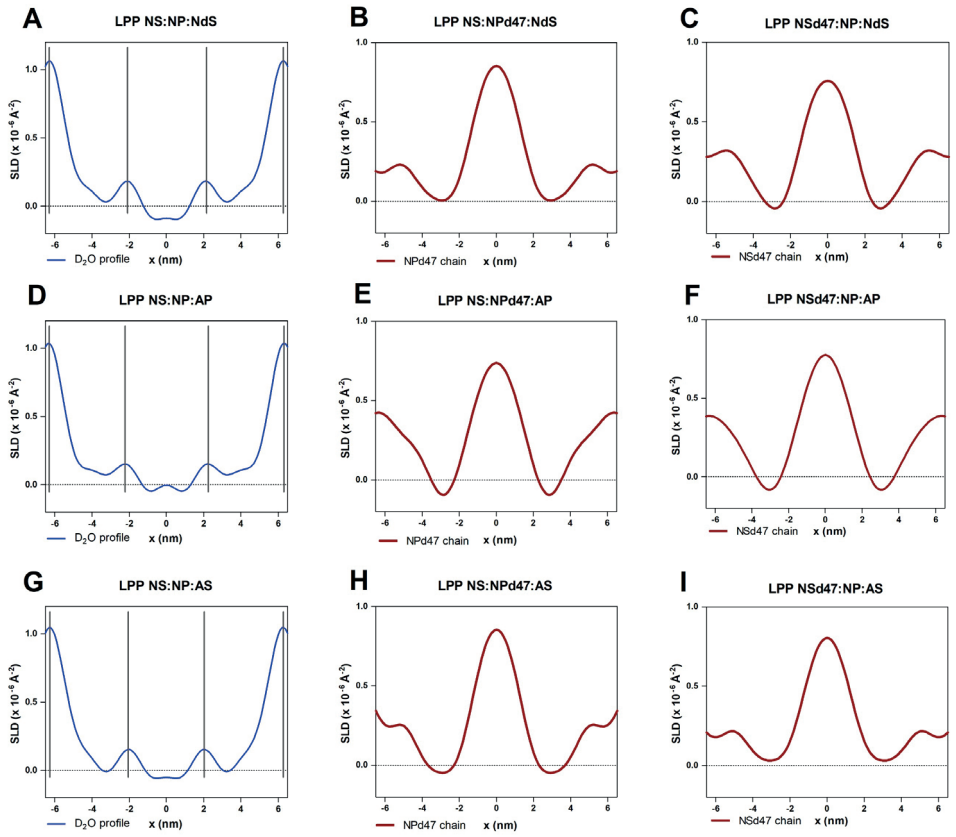

Figure 4. The neutron SLD profiles of the water (A, D, G), acyl chain of CER NP and acyl chain of CER NS in the LPP NS:NP:NdS (B,C), LPP NS:NP:AP (E,F) and LPP NS:NP:AS (H,I) models. The SLD water profiles are determined from the subtraction of the SLD profiles of the protiated sample measured at 8% D_2O/H_2O buffer hydration from the 100% D_2O/H_2O buffer. The vertical black lines (A, D, G) denote the localization of the water molecules in the LPP unit, thus also the lipid head groups position.

Lipid chain interactions

The lipid chain interactions were examined using the peak splitting of the δCD_2 and δCH_2 vibrations from the FTIR spectra (Figure 5). When the lipids form an orthorhombic packing, the CH_2 chains are densely packed, resulting in CH_2-CH_2 (or CD_2-CD_2) short-range coupling due to the proximity of the CH_2 (CD_2) groups. As a consequence, the scissoring

vibrations split into two peaks. The distance between two scissoring peaks is dependent on the size of the orthorhombic domains.

The δCH_2 and δCD_2 frequencies have a considerable vibrational energy variation (δCH_2 vibrations are between 1460 – 1480 cm^{-1} and the δCD_2 vibrations between 1080 – 1095 cm^{-1}). When the lipid domain size is around 100 chains, the maximum peak splitting is achieved (50, 51). If deuterated and protiated chains are in close proximity, CD_2-CH_2 interactions occur and because of the vibrational energy difference the CD_2-CD_2 chain interactions are lost. Such interactions result in a single peak at 1088 cm^{-1}. In combination with CD_2-CD_2 peak splitting, a larger peak at 1088 cm^{-1} leads to poorer peak separation of the two orthorhombic peaks and a smaller depth between the peaks.

In the LPP NS:NP 1:1 model previously investigated (CER EOS, CER NP, CER NS, CHOL and FFA C24), it was concluded that the acyl chains of CER NS and CER NP together with FFA C24 are all primarily located in the inner layer of the LPP trilayer unit (38). This is based on the localization of the CER NP and CER NS acyl chains from neutron diffraction measurements and FTIR (δCD_2 peak splitting distance of 6.4 ± 0.1 cm^{-1} for the lipid model with NSd47, NPd47 and DFFA – Table 4). Moreover, CER NS and CER NP adopted the linear conformation (with the acyl and sphingosine chain oriented on both sides of the CER headgroup). The neutron diffraction results presented above for the three models investigated in this study indicate a primary location of the acyl chains of CER NP and CER NS in the inner layer of the LPP unit cell as well. No information is available about the position of the acyl chains belonging to CER AP, CER AS or CER NdS as these deuterated CERs are not commercially available.

However, if CER AS, CER AP or CER NdS chains are partly located in the inner layer of the LPP, the δCD_2 peak splitting should be reduced, as protiated chains (sphingosine chains, acyl chains or both) will interfere with the CD_2-CD_2 chain interactions and consequently will reduce the deuterated domain size. The δCD_2 vibrations of the three models with deuterated NS and deuterated NP show a δCD_2 peak splitting distance between 5.3 – 5.5 cm^{-1} (Table 4). As a significant reduction in the δCD_2 peak splitting is observed compared to the LPP NS:NP 1:1 model (6.4 ± 0.1 cm^{-1}), these results suggest that there are more protiated lipid chains neighboring the deuterated chains of CER NP, CER NS and FFA in the LPP NSd47:NPd47:AS:DFFA, LPP NSd47:NPd47:AP:DFFA and LPP NSd47:NPd47:NdS:DFFA models compared to the LPP-NSd47-NPd47-DFFA model. As previous studies reported that CER NP and CER NS are arranged in a linear conformation in LPP lipid models, with the acyl chains and sphingoid bases placed on either side of the CER head group (in lipid models with different compositions, both simple and complex models) (29, 30, 38, 56), it is likely that this is the case for the models used in this study. Therefore, it is expected that the reduction in splitting is caused by the acyl or sphingosine chains of CER AS, CER AP and CER NdS located in the central layer. A clear conclusion cannot be drawn only based on these FTIR results, as other complementary techniques are needed to confirm which lipid chains are neighboring the CER NS and CER NP acyl chains and FFAs.

δCH_2 vibrations show a broad peak at ~1467 cm^{-1} for all three models, while in the LPP NSd47:NPd47:NdS:DFFA system there is also a small shoulder on the left side of the peak (Figure 5B). This suggests that a portion of the protiated lipid chains might be hexagonally packed. The chains forming the hexagonal packing are located in the boundary layers of the LPP.

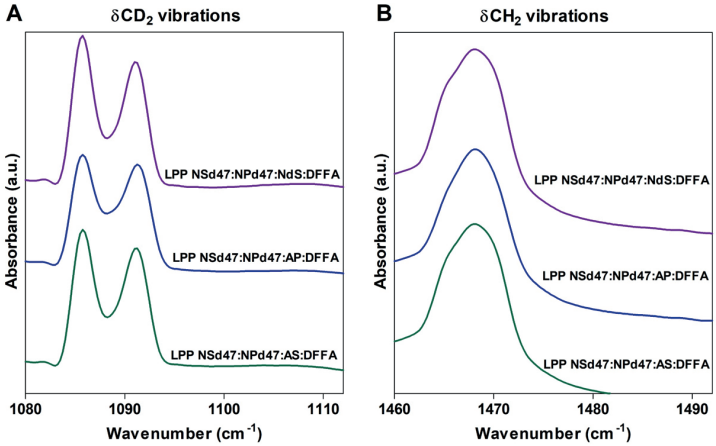

Figure 5. The δCD_2 vibrations (A) and δCH_2 vibrations (B) of the three partially deuterated models (10°C measurements). Deuterated FFA C24 and CER NS and CER NP with the deuterated acyl chain are included in these samples.

From the thermotropic curves of these three partially deuterated models (Figure S7) it can be observed that the protiated lipid chains undergo an orthorhombic – hexagonal phase transition, with the mid-transition temperatures shown in Table 5. The temperature ranges at which the transition takes place for the NdS and AS samples are smaller and sharper transitions can be observed, in contrast to the AP sample. The mid-transition temperatures are similar for the three models, both for the orthorhombic - hexagonal and hexagonal – liquid transitions (Table 4) and no significant differences were noted between the models. When comparing the thermotropic curve of the deuterated and protiated lipid chains, Figure S7 shows that the phase transitions occur in the same temperature ranges, for each model. This suggests that all lipids are well-mixed in the systems, part of the same lattice, as they are able to undergo phase transitions simultaneously.

Table 4. The splitting distance of the δCD_2 peak calculated at 10°C and the midpoint phase transition temperatures for the deuterated models. Data are presented as mean ± standard deviation of three measurements for each lipid composition.

Lipid sample	δCD_2 peak splitting distance (cm^{-1})	T_MO-H (°C)	T_MH-L (°C)
LPP NSd47:NPd47:AS:DFFA	5.4 ± 0.04	36.1 ± 0.8	63.9 ± 1.2
LPP NSd47:NPd47:AP:DFFA	5.5 ± 0.01	37.9 ± 1.5	66.7 ± 1.4
LPP NSd47:NPd47:NdS:DFFA	5.3 ± 0.01	39.8 ± 0.8	67.1 ± 1.2
LPP NS:NP 1:1 *	6.4 ± 0.1	-	-

* obtained from a previous study (38)

Lipid arrangement in a human ceramide model

The molecular arrangement in a lipid model with a composition mimicking the human SC was investigated as well. This model contains seven CER subclasses and a mix of FFAs with different chain lengths (Table 1) and it has the same lipid composition as used by Uche et al. (27). The SLD profiles corresponding to CER NP and CER NS with a deuterated acyl chain of were calculated as described above for the other lipid models. The two SLD profiles show high intensities in the inner part of the unit cell of the LPP (Figure S8 A,B). These results indicate that the acyl chains of CER NP and CER NS are predominantly located in the inner layer of the LPP, as was identified for the simple LPP models discussed above, as well as in previous studies (29, 30, 36, 38). The similar location of CER NS and CER NP in lipid models with various CER subclass composition complexity demonstrates the adaptability of the LPP structure to different CER head group compositions, indicating that the LPP lipid arrangement is insensitive to the CER composition.

Different models for the lipid arrangement in the LPP unit cell

Using neutron, X-ray diffraction and FTIR data, a model of the arrangement of the lipids in the LPP has been previously proposed, in which the acyl chains of the CERs and FFAs are predominantly located in the central layer, except the acyl chain of CER EOS, which is positioned in the two outer layers of the trilayer model together with the sphingoid chains and cholesterol, as represented in Figure S2 (29, 30, 36, 37, 58). As shown in this study and in previous papers, this model is consistent irrespective of whether a simpler lipid model (only containing CER EOS and CER NS subclasses) or a more complex lipid model (porcine CER and human CER model) is used (30, 37, 38). Using ruthenium tetroxide staining the SC lamellar organization was for the first time reported by Madison et al. (59). These studies showed broad-narrow-broad sequence of lucent bands in one repeating unit. Ruthenium tetroxide is a strong oxidizer that reacts with the double bonds of the lipid chains and the hydroxyl groups of the CERs (60). Thus, both the head groups and the linoleate position will turn into dark regions in the electron micrographs. Our proposed molecular arrangement is in agreement with the broad-narrow-broad lucent bands pattern reported.

The group of Norlen has studied the SC lamellar organization using cryo-electron microscopy. In their most recent paper two lamellar phases were reported, one with a repeat distance of 11-12 nm and a second one with a repeat distance of ~6 nm, which might represent the LPP and SPP (61). However, for the 11-12 nm phase, a two-layer asymmetric pattern was reported, which is not in agreement with the trilayer symmetric arrangement obtained using SAXD and Neutron diffraction (9, 30, 36, 37, 62).

Very recently another lipid arrangement has been proposed by Fandrei et al. for the simple LPP model with CER EOS and CER NS subclasses, based on NMR and neutron diffraction data (63). In that study, the assumption that the head groups of the lipids are located at the LPP unit cell boundary was disregarded and other phase signs were chosen for the structure factors during neutron data analysis. The newly proposed arrangement was mainly suggested based on the NMR findings of the isotropic linoleate tails of CER EOS. One of the essential differences between the model proposed previously in our papers and this new model by Fandrei et al. is the location of the acyl chain of CER EOS, which is positioned in the same layer as the acyl chains of CER NS and FFAs, with its isotropic linoleate forming the layer in the central part of the unit cell (63). Although this model is in accordance with respect to the NMR data, it raises the question whether such an isotropic fluid layer is in agreement with the high order displayed by X-ray diffraction patterns reported in their publication, but also in other studies, in which the various diffraction orders are very sharp indicating very ordered lamellar phases (9, 31, 63). It is important to mention that in the lipid models described by Fandrei et al. both the LPP and SPP are formed. However, the fraction of lipid classes in each of these phases cannot be quantified. As a result, the actual molar ratio between the lipids forming the LPP is not known. Another point of discussion is the permeability of the lipid model. In the model proposed by Fandrei et al. at a percentage of 30 m/m% CER EOS, the isotropic linoleate chains of CER EOS form a separate layer in the LPP. This would be expected to increase substantially the permeability of the lipid model compared to a model with a much lower concentration of CER EOS. However, it has been reported that a percentage of 10 mol% CER EOS (formation of both LPP and SPP) and 30% mol% CER EOS (formation of LPP exclusively) results in similar flux of ethyl-PABA across the membrane (10). It is important to note that in our lipid models the width of the δCD_2 splitting distance varies between 6.4 and 6.6 cm^{-1} and although the splitting distance is large, it is less than the maximum splitting distance of 7.4 cm^{-1} (29, 57). Whether this slight difference is due to a limited intercalation of protiated chains in the deuterated domains or the presence of disordered linoleate domains needs to be studied in future.

Further investigations are required to fully establish which model describes most accurately the lipid molecular arrangement in the LPP. Both models have in common the isotropic linoleate domains and the linear arrangement of the CERs. Calculating the neutron diffraction data obtained in this study with the phase signs used by Fandrei et al. (63) shows that in that model the acyl chains of both CER NS and CER NP still have the

same position in the LPP unit cell (Figure S9). This indicates that the conclusions of the present study regarding the adaptability of the lamellar structure to variations in the CER head groups are also translatable to this recently proposed lipid arrangement.

CONCLUSION

This study demonstrates that the lipid molecular arrangement in the unit cell of the LPP is insensitive to differences in the head group structure of the CERs and the complexity of the lipid model. Addition of either CER AS, CER NdS or CER AS in an LPP model along CER EOS, CER NP, CER NS, CHOL and FFA C24 did not change the acyl chain position of CER NP and CER NS or the lipid organization, however, it affected the TEWL, the hydrogen bond network of the models and the lateral packing, due to the different CER head group architecture. The lipid chain interactions investigated with FTIR suggest that CER AS, CER AP and CER NdS are located in the central layer of the LPP. The position of the acyl chains of CER NP and CER NS in the LPP unit cell is also similar in a complex lipid model that mimics the CER subclass composition of human SC and it is in agreement with previous reports.

ACKNOWLEDGEMENTS

We thank Prof. Dr. David Barlow and Prof. Dr. M. Jayne Lawrence (University of Manchester, U.K.) for the collaboration and critically reading the manuscript. We are thankful to Evonik (Essen, Germany) for donating the CERs utilized in this study. We would like to thank ISIS Neutron and Muon Source (Didcot, United Kingdom), Institut Laue-Langevin (Grenoble, France) and ALBA Synchrotron (Cerdanyola del Vallès, Spain) for the experimental beam time to perform the neutron and X-ray scattering measurements. ISIS neutron diffraction data DOI: 10.5286/ISIS.E.RB1969003-1 (53) and DOI: 10.5286/ISIS.E.RB2069000-1 (54). ILL neutron diffraction data DOI: 10.5291/ILL-DATA.9-13-939 (55). This study was financially supported by the National Institutes of Health (National Institute of Arthritis and Muscoskeletal and Skin Diseases), grant number R01AR072679.

REFERENCES

1. Menon, G. K., Cleary, G. W., Lane, M. E. (2012). The structure and function of the stratum corneum. *Int J Pharm*. 435(1), 3-9.
2. Proksch, E., Brandner, J. M., Jensen, J.-M. (2008). The skin: an indispensable barrier. *Experimental Dermatology*. 17(12), 1063-72.
3. Wertz, P. W., Miethke, M. C., Long, S. A., Strauss, J. S., Downing, D. T. (1985). The composition of the ceramides from human stratum corneum and from comedones. *J Invest Dermatol*. 84(5), 410-2.
4. Weerheim, A., Ponec, M. (2001). Determination of stratum corneum lipid profile by tape stripping in combination with high-performance thin-layer chromatography. *Arch Dermatol Res*. 293, 191-9.
5. Ponec, M., Weerheim, A., Lankhorst, P., Wertz, P. (2003). New Acylceramide in Native and Reconstructed Epidermis. *J Invest Dermatol*. 120(4), 581-8.
6. Hannun, Y. A., Obeid, L. M. (2008). Principles of bioactive lipid signalling: lessons from sphingolipids. *Nat Rev Mol Cell Biol*. 9(2), 139-50.
7. Kawana, M., Miyamoto, M., Ohno, Y., Kihara, A. (2020). Comparative profiling and comprehensive quantification of stratum corneum ceramides in humans and mice by LC/MS/MS. *J Lipid Res*. 61(6), 884-95.
8. White, S. H., Mirejovsky, D., King, G. I. (1988). Structure of Lamellar Lipid Domains and Corneocyte Envelopes of Murine Stratum Corneum. An X-ray Diffraction Study. *Biochemistry*. 27, 3725-32.
9. Bouwstra, J. A., Gooris, G. S., van der Spek, J. A., Bras, W. (1991). Structural investigations of human stratum corneum by small-angle X-ray scattering. *J Invest Dermatol*. 97(6), 1005-12.
10. Uche, L. E., Gooris, G. S., Bouwstra, J. A., Beddoes, C. M. (2021). High concentration of the ester-linked omega-hydroxy ceramide increases the permeability in skin lipid model membranes. *Biochim Biophys Acta Biomembr*. 1863(1), 183487.
11. Opalka, L., Kovacik, A., Pullmannova, P., Maixner, J., Vavrova, K. (2020). Effects of omega-O-acylceramide structures and concentrations in healthy and diseased skin barrier lipid membrane models. *Journal of lipid research*. 61(2), 219-28.
12. Opálka, L., Meyer, J. M., Ondrejčeková, V., Svatošová, L., Radner, F. P. W., Vávrová, K. (2022). ω-O-Acylceramides but not ω-hydroxy ceramides are required for healthy lamellar phase architecture of skin barrier lipids. *J Lipid Res*. 63(6), 100226.
13. Bouwstra, J. A., Gooris, G. S., Dubbelaar, F. E., Weerheim, A., IJzerman, A. P., Ponec, M. (1998). Role of ceramide 1 in the molecular organization of the stratum corneum lipids. *J Lipid Res*. 39, 186-96.
14. Kovacik, A., Silarova, M., Pullmannova, P., Maixner, J., Vavrova, K. (2017). Effects of 6-Hydroxyceramides on the Thermotropic Phase Behavior and Permeability of Model Skin Lipid Membranes. *Langmuir*. 33(11), 2890-9.
15. Kovacik, A., Vogel, A., Adler, J., Pullmannova, P., Vavrova, K., Huster, D. (2018). Probing the role of ceramide hydroxylation in skin barrier lipid models by (2)H solid-state NMR spectroscopy and X-ray powder diffraction. *Biochim Biophys Acta Biomembr*. 1860(5), 1162-70.
16. Pullmannova, P., Ermakova, E., Kovacik, A., Opalka, L., Maixner, J., Zbytovska, J., et al. (2019). Long and very long lamellar phases in model stratum corneum lipid membranes. *J Lipid Res*. 60(5), 963-71.
17. Pullmannova, P., Curikova-Kindlova, B. A., Ondrejcekova, V., Kovacik, A., Dvorakova, K., Dulanska, L., et al. (2023). Polymorphism, Nanostructures, and Barrier Properties of Ceramide-Based Lipid Films. *ACS Omega*. 8(1), 422-35.
18. Mendelsohn, R., Rerek, M. E., Moore, D. J. (2000). Infrared spectroscopy and microscopic imaging of stratum corneum models and skin. *Physical Chemistry Chemical Physics*. 2(20), 4651-7.
19. Boncheva, M., Damien, F., Normand, V. (2008). Molecular organization of the lipid matrix in intact Stratum corneum using ATR-FTIR spectroscopy. *Biochim Biophys Acta*. 1778(5), 1344-55.
20. Damien, F., Boncheva, M. (2010). The extent of orthorhombic lipid phases in the stratum corneum determines the barrier efficiency of human skin in vivo. *J Invest Dermatol*. 130(2), 611-4.
21. Björklund, S., Nowacka, A., Bouwstra, J. A., Sparr, E., Topgaard, D. (2013). Characterization of Stratum Corneum Molecular Dynamics by Natural-Abundance 13C Solid-State NMR. *PLoS One*. 8(4), e61889.
22. Bouwstra, J., Gooris, G., Cheng, K., A., W., Bras, W., Ponec, M. (1996). Phase behavior of isolated skin lipids. *J Lipid Res*. 37, 999 - 1011.
23. McIntosh, T. J., Stewart, M. E., Downing, D. T. (1996). X-ray Diffraction Analysis of Isolated Skin Lipids: Reconstitution of Intercellular Lipid Domains. *Biochemistry*. 35(12), 3649-53.
24. Bouwstra, J. A., Gooris, G. S., Dubbelaar, F. E. R., Ponec, M. (2001). Phase behavior of lipid mixtures based on human ceramides: coexistence of crystalline and liquid phases. *J Lipid Res*. 42(11), 1759-70.

25. de Jager, M. W., Gooris, G. S., Ponec, M., Bouwstra, J. A. (2005). Lipid mixtures prepared with well-defined synthetic ceramides closely mimic the unique stratum corneum lipid phase behavior. *J Lipid Res*. 46(12), 2649-56.
26. Opalka, L., Kovacik, A., Maixner, J., Vavrova, K. (2016). Omega-O-Acylceramides in Skin Lipid Membranes: Effects of Concentration, Sphingoid Base, and Model Complexity on Microstructure and Permeability. *Langmuir*. 32(48), 12894-904.
27. Uche, L. E., Gooris, G. S., Bouwstra, J. A., Beddoes, C. M. (2019). Barrier Capability of Skin Lipid Models: Effect of Ceramides and Free Fatty Acid Composition. *Langmuir*. 35(47), 15376-88.
28. Janssens, M., Gooris, G. S., Bouwstra, J. A. (2009). Infrared spectroscopy studies of mixtures prepared with synthetic ceramides varying in head group architecture: coexistence of liquid and crystalline phases. *Biochim Biophys Acta*. 1788(3), 732-42.
29. Beddoes, C. M., Gooris, G. S., Bouwstra, J. A. (2018). Preferential arrangement of lipids in the long-periodicity phase of a stratum corneum matrix model. *J Lipid Res*. 59(12), 2329-38.
30. Beddoes, C. M., Gooris, G. S., Foglia, F., Ahmadi, D., Barlow, D. J., Lawrence, M. J., et al. (2020). Arrangement of Ceramides in the Skin: Sphingosine Chains Localize at a Single Position in Stratum Corneum Lipid Matrix Models. *Langmuir*. 36(34), 10270-8.
31. Gooris, G. S., Kamran, M., Kros, A., Moore, D. J., Bouwstra, J. A. (2018). Interactions of dipalmitoylphosphatidylcholine with ceramide-based mixtures. *Biochim Biophys Acta Biomembr*. 1860(6), 1272-81.
32. Badhe, Y., Schmitt, T., Gupta, R., Rai, B., Neubert, R. H. H. (2022). Investigating the nanostructure of a CER[NP]/CER[AP]-based stratum corneum lipid matrix model: A combined neutron diffraction & molecular dynamics simulations approach. *Biochim Biophys Acta Biomembr*. 1864(10), 184007.
33. Moore, T. C., Iacovella, C. R., Leonhard, A. C., Bunge, A. L., McCabe, C. (2018). Molecular dynamics simulations of stratum corneum lipid mixtures: A multiscale perspective. *Biochemical and Biophysical Research Communications*. 498(2), 313-8.
34. Moore, T. C., Hartkamp, R., Iacovella, C. R., Bunge, A. L., McCabe, C. (2018). Effect of Ceramide Tail Length on the Structure of Model Stratum Corneum Lipid Bilayers. *Biophys J*. 114(1), 113-25.
35. Shamaprasad, P., Moore, T. C., Xia, D., Iacovella, C. R., Bunge, A. L., McAbe, C. (2022). Multiscale Simulation of Ternary Stratum Corneum Lipid Mixtures: Effects of Cholesterol Composition. *Langmuir*. 38(24), 7496-511.
36. Mojumdar, E. H., Gooris, G. S., Barlow, D. J., Lawrence, M. J., Deme, B., Bouwstra, J. A. (2015). Skin lipids: localization of ceramide and fatty acid in the unit cell of the long periodicity phase. *Biophys J*. 108(11), 2670-9.
37. Mojumdar, E. H., Gooris, G. S., Groen, D., Barlow, D. J., Lawrence, M. J., Deme, B., et al. (2016). Stratum corneum lipid matrix: Location of acyl ceramide and cholesterol in the unit cell of the long periodicity phase. *Biochim Biophys Acta*. 1858(8), 1926-34.
38. Nădăban, A., Gooris, G. S., Beddoes, C. M., Dalgliesh, R. M., Bouwstra, J. A. (2022). Phytosphingosine ceramide mainly localizes in the central layer of the unique lamellar phase of skin lipid model systems. *J Lipid Res*. 63(9), 100258.
39. Wojdyr, M. (2010). Fityk: a general-purpose peak fitting program. *Journal of Applied Crystallography*. 43(5), 1126-8.
40. Oguri, M., Gooris, G. S., Bito, K., Bouwstra, J. A. (2014). The effect of the chain length distribution of free fatty acids on the mixing properties of stratum corneum model membranes. *Biochim Biophys Acta*. 1838(7), 1851-61.
41. Arnold, O., Bilheux, J. C., Borreguero, J. M., Buts, A., Campbell, S. I., Chapon, L., et al. (2014). Mantid—Data analysis and visualization package for neutron scattering andμSR experiments. *Nuclear Instruments and Methods in Physics Research Section A: Accelerators, Spectrometers, Detectors and Associated Equipment*. 764, 156-66.
42. Franks, N. P., Lieb, W.R. (1979). The Structure of Lipid Bilayers and the Effects of General Anaesthetics: An X-ray and Neutron Diffraction Study. *J Mol Biol*. 133, 469-500.
43. NIST Center of Neutron Research. https://www.ncnr.nist.gov/resources/activation/, 2022 (accessed 1 February 2022).
44. Wiener, M. K., G.; White, S. (1991). Structure of a fluid dioleoylphosphatidylcholine bilayer determined by joint refinement of x-ray and neutron diffraction data 1. Scaling of neutron data and the distributions of double bonds and water. *Biophys J*. 60, 568-76.
45. Beddoes, C. M., Gooris, G. S., Barlow, D. J., Lawrence, M. J., Dalgliesh, R. M., Malfois, M., et al. (2022). The importance of ceramide headgroup for lipid localisation in skin lipid models. *Biochim Biophys Acta Biomembr*. 1864(6), 183886.

46. Gonthier, J., Barrett, M. A., Aguettaz, O., Baudoin, S., Bourgeat-Lami, E., Demé, B., et al. (2019). BerILL: The ultimate humidity chamber for neutron scattering. *Journal of Neutron Research*. 21, 65-76.
47. Richard, D., Ferrand, M., Kearley, G. J. (1996). Analysis and Visualisation of Neutron Scattering Data. *Journal of Neutron Research*. 4, 33-9.
48. Uche, L. E., Gooris, G. S., Beddoes, C. M., Bouwstra, J. A. (2019). New insight into phase behavior and permeability of skin lipid models based on sphingosine and phytosphingosine ceramides. *Biochim Biophys Acta Biomembr*. 1861(7), 1317-28.
49. Moore, D. J., Rerek, M. E., Mendelsohn, R. (1997). Lipid Domains and Orthorhombic Phases in Model Stratum Corneum: Evidence from Fourier Transform Infrared Spectroscopy Studies. *Biochemical and Biophysical Research Communications*. 231, 797 - 801.
50. Mendelsohn, R., Moore, D. J. (1998). Vibrational spectroscopic studies of lipid domains in biomembranes and model systems. *Chem Phys Lipids*. 96, 141-57.
51. Moore, D. J., Rerek, M. E., Mendelsohn, R. (1997). FTIR Spectroscopy Studies of the Conformational Order and Phase Behavior of Ceramides. *J Phys Chem B*. 101, 8933-40.
52. Moore, D. J., Rerek, M. E., Mendelsohn, R. (1999). Role of ceramides 2 and 5 in the structure of the stratum corneum lipid barrier. *Int J Cosmet Sci*. 21(5), 353-68.
53. Rerek, M. E., Chen, H., Markovic, B., Van Wyck, D., Garidel, P., Mendelsohn, R., et al. (2001). Phytosphingosine and Sphingosine Ceramide Headgroup Hydrogen Bonding: Structural Insights through Thermotropic Hydrogen/Deuterium Exchange. *J Phys Chem B*. 105, 9355 - 62.
54. Mojumdar, E. H., Kariman, Z., van Kerckhove, L., Gooris, G. S., Bouwstra, J. A. (2014). The role of ceramide chain length distribution on the barrier properties of the skin lipid membranes. *Biochim Biophys Acta*. 1838(10), 2473-83.
55. Kovacik, A., Pullmannova, P., Opalka, L., Silarova, M., Maixner, J., Vavrova, K. (2021). Effects of (R)- and (S)-alpha-Hydroxylation of Acyl Chains in Sphingosine, Dihydrosphingosine, and Phytosphingosine Ceramides on Phase Behavior and Permeability of Skin Lipid Models. *Int J Mol Sci*. 22(14).
56. Nădăban, A., Rousel, J., El Yachioui, D., Gooris, G. S., Beddoes, C. M., Dalgliesh, R. M., et al. (2023). Effect of sphingosine and phytosphingosine ceramide ratio on lipid arrangement and barrier function in skin lipid models. *J Lipid Res*. 64(8), 100400.
57. Uche, L. E., Gooris, G. S., Bouwstra, J. A., Beddoes, C. M. (2021). Increased Levels of Short-Chain Ceramides Modify the Lipid Organization and Reduce the Lipid Barrier of Skin Model Membranes. *Langmuir*. 37(31), 9478-89.
58. Groen, D., Gooris, G. S., Barlow, D. J., Lawrence, M. J., van Mechelen, J. B., Deme, B., et al. (2011). Disposition of ceramide in model lipid membranes determined by neutron diffraction. *Biophys J*. 100(6), 1481-9.
59. Madison, K. C., Swartzendruber, D. C., Wertz, P. W., Downing, D. T. (1987). Presence of intact intercellular lipid lamellae in the upper layers of the stratum corneum. *J Invest Dermatol*. 88(6), 714-8.
60. Hill, J. R., Wertz, P. W. (2003). Molecular models of the intercellular lipid lamellae from epidermal stratum corneum. *Biochimica et Biophysica Acta (BBA) - Biomembranes*. 1616(2), 121-6.
61. Narangifard, A., Wennberg, C. L., den Hollander, L., Iwai, I., Han, H., Lundborg, M., et al. (2021). Molecular Reorganization during the Formation of the Human Skin Barrier Studied In Situ. *J Invest Dermatol*. 141(5), 1243-53 e6.
62. Groen, D., Gooris, G. S., Bouwstra, J. A. (2009). New insights into the stratum corneum lipid organization by X-ray diffraction analysis. *Biophys J*. 97(8), 2242-9.
63. Fandrei, F., Havrisak, T., Opalka, L., Engberg, O., Smith, A. A., Pullmannova, P., et al. (2023). The intriguing molecular dynamics of Cer[EOS] in rigid skin barrier lipid layers requires improvement of the model. *J Lipid Res*. 64(5), 100356.
64. Bouwstra, J., Gooris, G., Dalgliesh, R. M., Beddoes, C. M., Nădăban, A. (2020) Understanding the effect of Ceramide NP concentration on the skin's long periodicity phase - relevant for atopic eczema studies. DOI: https://doi.org/10.5286/ISIS.E.RB1969003.
65. Bouwstra, J. A., Beddoes, C. M., Nădăban, A., Dalgliesh, R. M., Gooris, G. S. (2020) The effect of ceramide head group on the lipid organization in the long periodicity phase of stratum corneum substitutes. STFC ISIS Neutron and Muon Source. DOI: https://doi.org/10.5286/ISIS.E.RB2069000.
66. Lawrence, M. J., Barlow, D. J., Beddoes, C. M., Deme, B., Gooris, G. S., Nădăban, A. (2021) Investigating the molecular basis of inflammatory skin conditions. Institut Laue-Langevin (ILL). DOI: https://doi.org/10.5291/ILL-DATA.9-13-939.

SUPPLEMENTAL INFORMATION

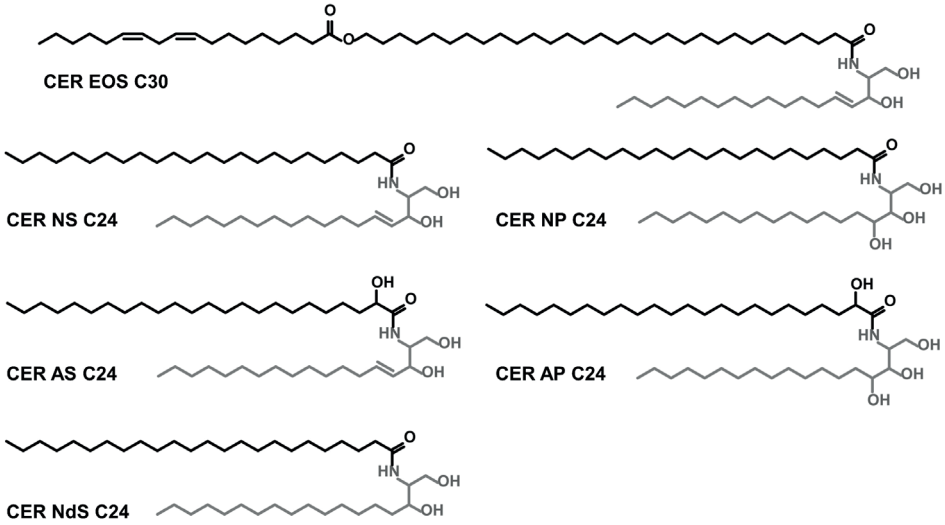

Figure S1. The CERs included in the lipid compositions and their structures.

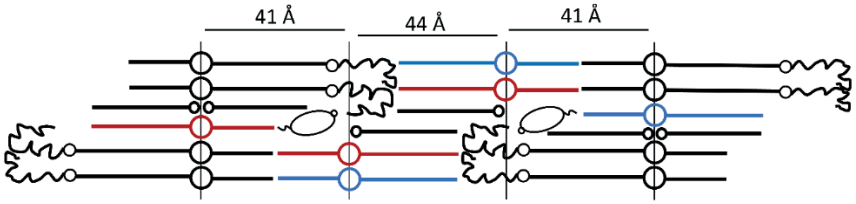

Figure S2. The molecular arrangement of lipids in the LPP unit cell trilayer, in a model with the composition CER EOS C30: CER NS C24: CER NP C24: CHOL: FFA C24 (molar ratio 0.4:0.3:0.3:1:1). Reprinted from Nădăban et al. (1). CER NS is highlighted in red and CER NP in blue, whereas CER EOS, FFA C24 and CHOL are in black.

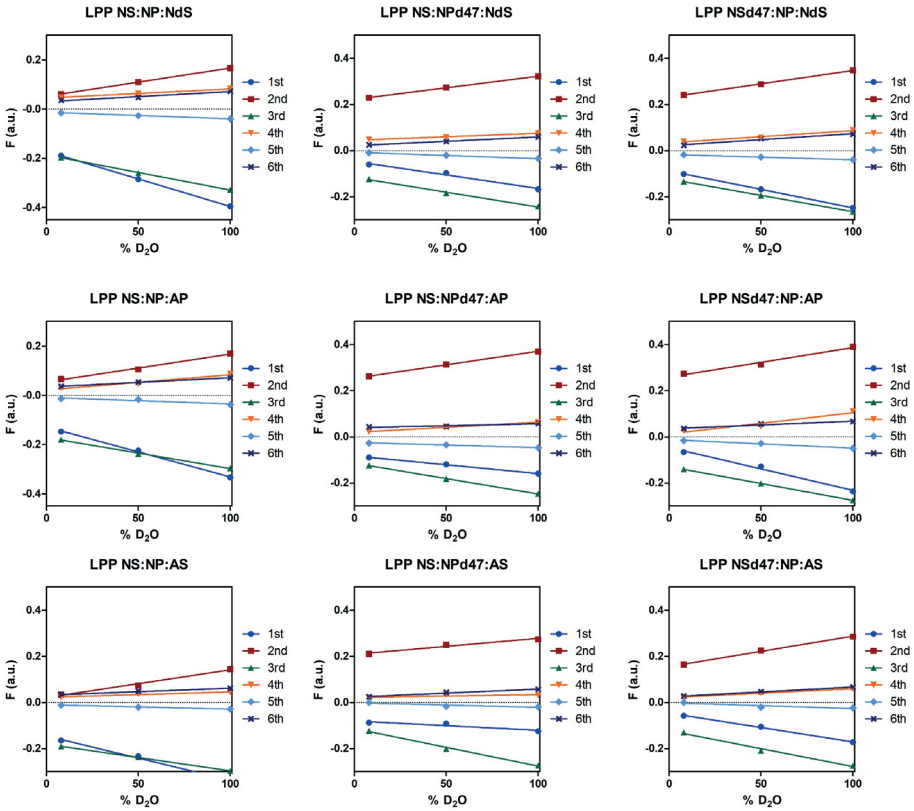

Figure S3. Linear correlation of the structure factors with the D_2O percentage (in the D_2O/H_2O buffer) of the six diffraction orders of the LPP models LPP NS:NP:NdS, LPP NS:NP:AP and LPP NS:NP:AS. Each diffraction order is indicated by different colors and symbols: first (square, dark blue), second (triangle, red), third (diamond, green), fourth (dot, orange), fifth (triangle, light blue), sixth (cross, grey).

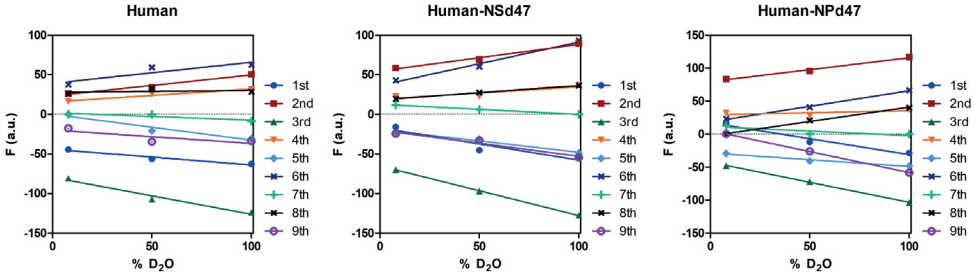

Figure S4. Linear correlation of the structure factors with the D_2O/H_2O hydration level for the protiated Human model, Human-NSd47 (with the deuterated CER NS acyl chain) and Human-NPd47 model (with the deuterated CER NP acyl chain). Each diffraction order is indicated by different colors and symbols: first (square, dark blue), second (triangle, red), third (diamond, green), fourth (dot, orange), fifth (triangle, light blue), sixth (cross, grey), seventh (plus, light green), eighth (cross, black) and ninth (circle, magenta).

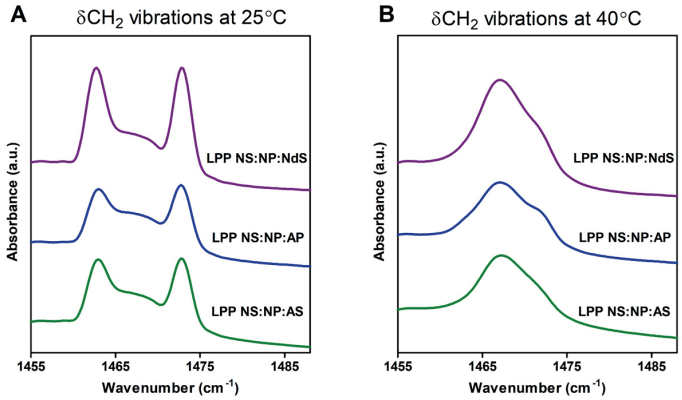

Figure S5. The CH_2 scissoring vibrations of the LPP NS:NP:NdS, LPP NS:NP:AP and LPP NS:NP:AS, measured by FTIR at 25°C and 40°C. The lipid model name is indicated on each curve.

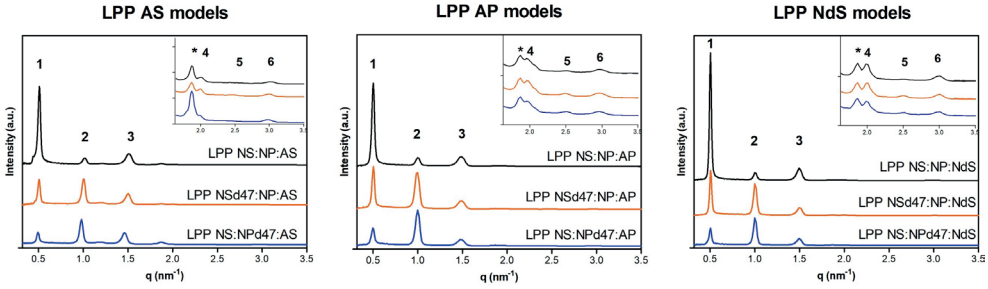

Figure S6. One-dimensional neutron scattering plots for the three models (LPP NS:NP:AS, LPP NS:NP:AP and LPP NS:NP:NdS), protiated and deuterated, at 100% D_2O/H_2O buffer ratio. The inserted cassette displays a zoom-in of the scattering vector (q) region 1.7 - 3.5 nm^{-1}. The six diffraction orders corresponding to the LPP are denoted with numbers and the phase-separated CHOL diffraction peak is marked with an asterisk.

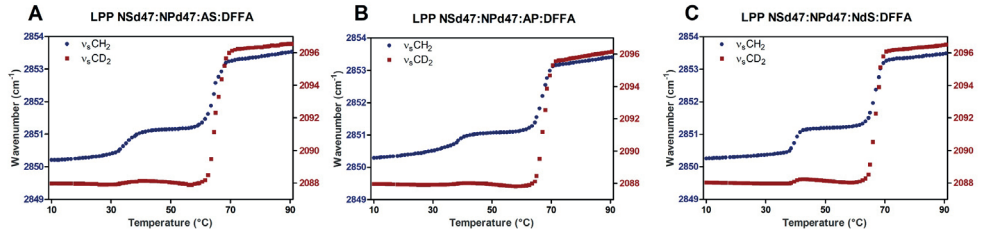

Figure S7. The ν_sCH_2 and ν_sCD_2 thermotropic curves of the three lipid systems that include the deuterated CER NS and CER NP acyl chains and DFFA (LPP NSd47:NPd47:AS:DFFA, LPP NSd47:NPd47:AP:DFFA and LPP NSd47:NPd47:NdS:DFFA). The wavenumbers of the ν_sCH_2 and ν_sCD_2 peak positions (left and right y-axis) are plotted in the 10-90°C temperature range. An average of three separate measurements per lipid sample is plotted in the graphs.

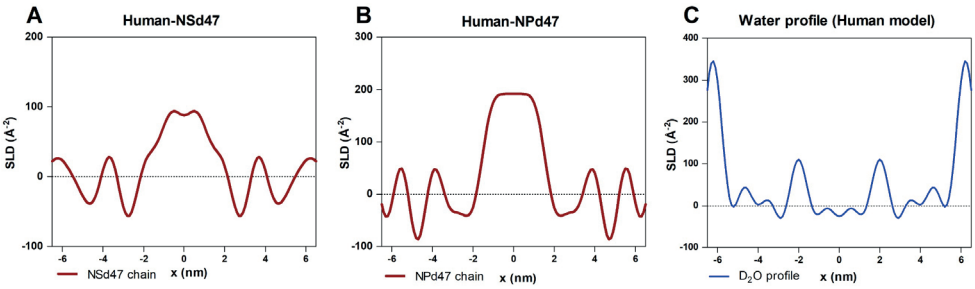

Figure S8. The net neutron SLD profile of the of the deuterated CER NS47 acyl chain (A) and CER NPd47 acyl chain (B) in the human complex model and the water profile of the human model (C). The net SLD profiles of the NSd47 and NPd47 chains display high intensities in the inner part of the LPP unit cell (B,C). The profiles also show other elevations in intensity at ~4.1 nm from the unit cell center, however these can be attributed to the truncation of the data due to data processing.

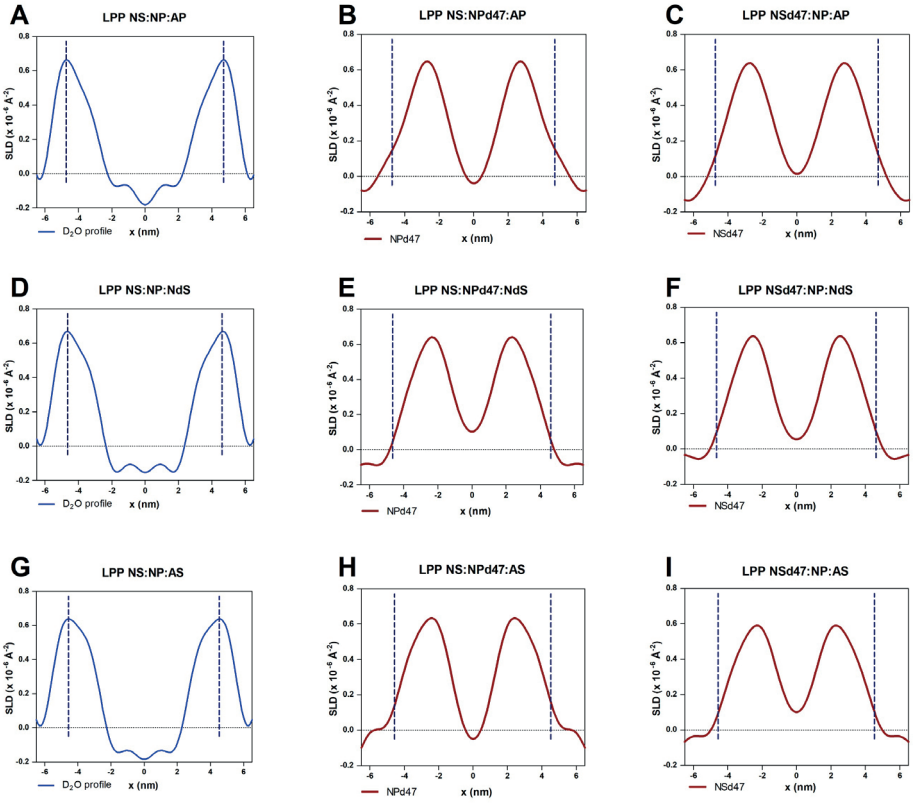

Figure S9. The neutron SLD profiles of the water (A, D, G), acyl chain of CER NP and acyl chain of CER NS in the LPP NS:NP:AP (B,C), LPP NS:NP:NdS (E,F) and LPP NS:NP:AS (H,I) models. These SLD profiles are calculated according to the method suggested by Fandrei et al. (2), with the most suitable phase sign combination for the six diffraction orders (- - + - + -). The SLD profile of the water shows the peak position at ~4.4 nm from unit cell center, indicating the lipid headgroup location. The position of the headgroup region in each sample is indicated by the black dotted line.

SUPPLEMENTARY REFERENCES:

1. Nădăban, A., Gooris, G. S., Beddoes, C. M., Dalgliesh, R. M., Bouwstra, J. A. (2022). Phytosphingosine ceramide mainly localizes in the central layer of the unique lamellar phase of skin lipid model systems. J Lipid Res. 63(9), 100258.
2. Fandrei, F., Havrisak, T., Opalka, L., Engberg, O., Smith, A. A., Pullmannova, P., et al. (2023). The intriguing molecular dynamics of Cer[EOS] in rigid skin barrier lipid layers requires improvement of the model. J Lipid Res. 64(5), 100356.